

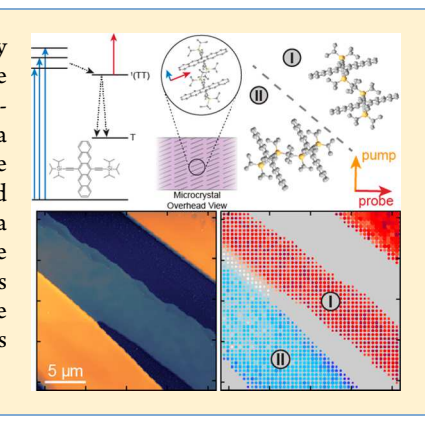
Multidimensional Spectroscopy on the Microscale: Development of a Multimodal Imaging System Incorporating 2D White-Light Spectroscopy, Broadband Transient Absorption, and Atomic Force Microscopy

Published as part of The Journal of Physical Chemistry virtual special issue "Time-Resolved Microscopy".

Andrew C. Jones, Nicholas M. Kearns, Miriam Bohlmann Kunz, Jessica T. Flach, and Martin T. Zanni*®

Department of Chemistry, University of Wisconsin, Madison, Wisconsin 53706, United States

ABSTRACT: The dynamics of electronic transitions in solid-state materials are closely linked to microscopic morphology, but it is challenging to simultaneously characterize their spectral and temporal response with high spatial resolution. We present a timeresolved nonlinear microscopy system using white-light supercontinuum pulses as a broadband light source. This system is capable of correlating nanometer scale sample morphology determined from atomic force topography measurements with broadband transient absorption hyperspectral images and ultrafast 2D white-light spectra, all with a spatial resolution of $\leq 1 \mu m$. The experimental apparatus is described with a focus on the dispersion management strategies necessary to minimize the duration of optical pulses when implementing an AOM based pulse-shaping system covering a broad-spectral range in the VIS/NIR. Experiments on TIPS-pentacene organic semiconductor microcrystals are used to demonstrate the unique capabilities of this technique.



1. INTRODUCTION

Transient absorption (TA) microscopy and two-dimensional electronic spectroscopy (2DES) have proven to be valuable tools for the measurement of the dynamics associated with electronic transitions throughout the visible spectral range. 1-4 Transient absorption measurements provide access to the inherent time scales which govern a system's response to photoexcitation including energy/charge transfer, diffusion, decay, and conversion processes among others. By resolving the correlation between the optical excitation energy and response energies, 2DES techniques further provide a means of tracking couplings and energy transfer processes between multiple electronic excitations. Through implementation of a 4-f Acousto-optic modulator (AOM) based pulse shaping system, we detail the development of a multimodal microscopy system capable of combining the temporal and spatial resolution available from TA microscopy mapping with the broad spectral bandwidths and multidimensional characterization capabilities available from 2DES.

As many electronic transitions in condensed phase and solidstate materials span optical bandwidths of tens of nanometers, in order to characterize couplings and energy transfer processes between multiple electronic transitions, it is advantageous to utilize light sources which are as spectrally broad as 2DES experiments are naturally suited for characterization of these broad absorption features as large bandwidth optical pulses are employed as a means of resolving the optical response corresponding to excitation and probe optical pulses across each axis of the 2D spectra. Moreover, as electronic transitions can also be associated with fast ~femtosecond dephasing times, it is further necessary that both pump and probe pulses be temporally compressed to resolve the intrinsic system dynamics. Such compression, however, represents a challenge for broadband optical pulses in the visible spectral range, as most transmissive materials present in the experimental beampath are highly dispersive, necessitating the need for precise correction of large magnitudes of spectral phase variation.

Broadband TA microscopy techniques have been demonstrated using nondegenerate, spectrally narrow bandwidth pump and probe pulses in order to reduce the temporal stretching associated with dispersive, transmissive microscope objectives. 15-18 This constraint limits measurements to excitation and probing of singular and spectrally separate electronic transitions. In contrast, 2DES measurements typically provide information on the transient spectral response covering a broad, spectrally degenerate bandwidth for the pump and probe pulses. These techniques, however, are generally implemented without appreciable spatial resolution. Avoiding the use of dispersive microscope objectives, 2DES characterization has been limited to spatial resolutions of at best $\gtrsim 10 \ \mu \text{m.}^{19}$ This resolution represents a significant

Received: September 25, 2019 Revised: November 3, 2019 Published: November 7, 2019

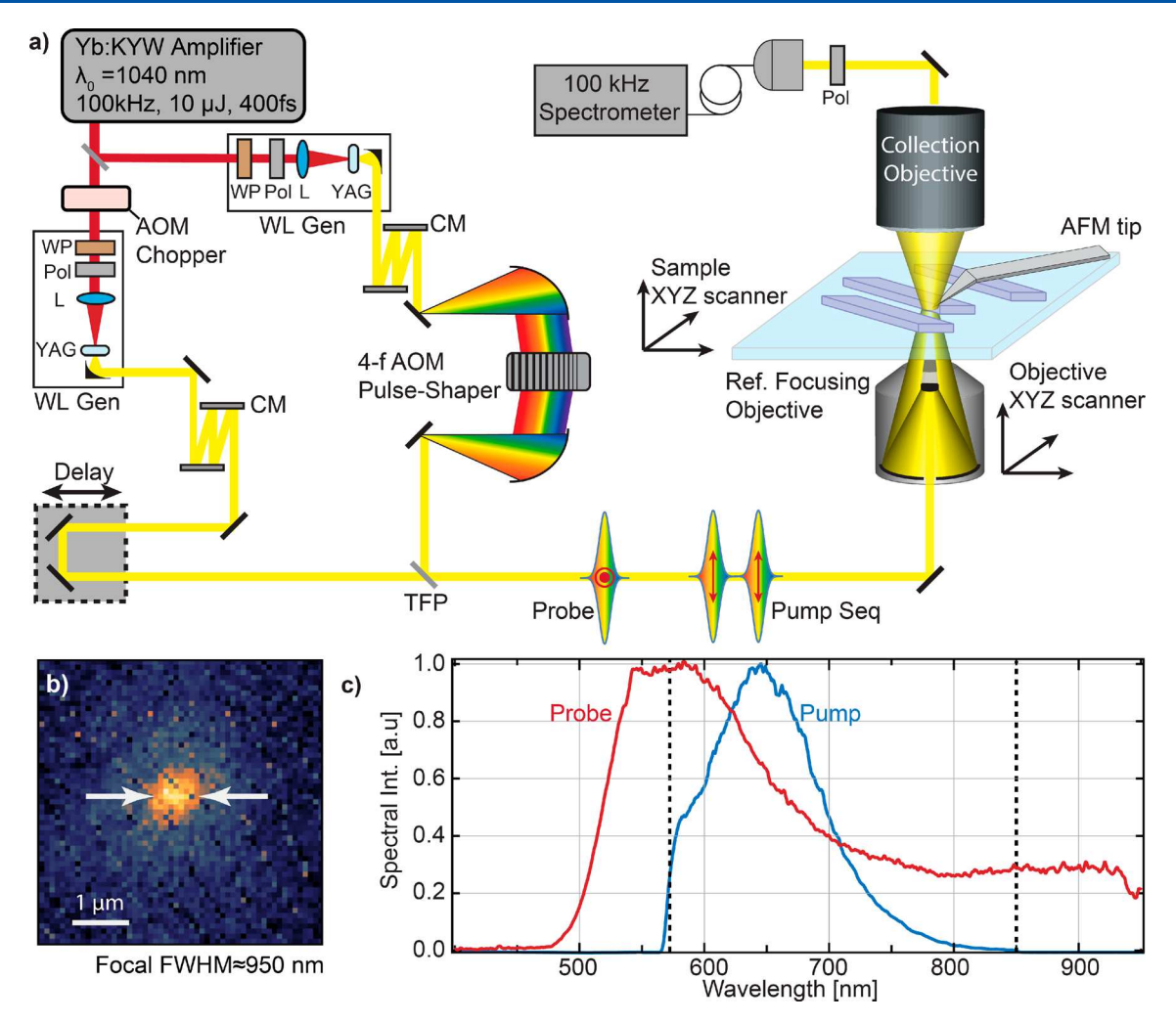


Figure 1. (a) Experimental schematic of the 2DWL microscopy system. WL generation is performed by sending the fundamental laser source through a waveplate (WP)/polarizer (pol) variable attenuator, and focusing via a 75 mm focal length lens (L) into a YAG crystal. Chirped mirrors (CM) and the AOM pulse-shaper are used for dispersion compensation while a thin-film polarizer is used to combine pump and probe beams prior to the microscope. (b) Image of the intensity distribution of the WL supercontinuum transduced via deflection of the AFM probe in contact with the sample surface. (c) Representative spectral distributions of the pump and probe pulses incident upon the sample. The dashed vertical lines indicate the limiting wavelengths diffracted by the acoustic aperture of a TeO₂ AOM pulse-shaper.

limitation, as the photoresponse of a material is often closely linked to microscopic morphology below this resolution.

Following our initial report,²⁰ we detail the experimental combination of broadband 2DES spectroscopy with TA microscopy to create a multimodal two-dimensional whitelight (2DWL) microscopy system. The apparatus in question combines an atomic force microscope (AFM) providing nanometer-scale topographic resolution, a confocal optical microscope, and the pulse-shaping/phase control of a 2DWL spectroscopy system. As an optical source for both the pump excitation and probe detection, we implement broadband white-light (WL) supercontinuum generation to create pulses >200 nm in spectral bandwidth. The addition of pulseshaping^{6,21,22} further enables creation of user-defined pulsepair sequences with well-defined temporal separation and relative phase. The advantage here is twofold: 2DES measurements can be performed using the same "pumpprobe" experimental geometry as TA measurements, 23,24 while the third-order signal pathways of interest may be extracted using a combination of polarization control and phase-cycling of the pulse-sequence. 21,25,26

While use of a pulse-shaping system greatly simplifies the experimental geometry of 2DES measurements, implementing these techniques over broad-bandwidths requires overcoming challenges associated with the intrinsic dispersion of the shaper itself, particularly for the visible spectral range. In the following sections, we detail the specifics of our experimental apparatus, the signal-to-noise gains associated with utilizing shot-to-shot pulse-shaping/detection, and dispersion compensation strategies for the implementation of an AOM pulse-shaping system operating over broad optical bandwidths. As a demonstration, we perform ultrafast spectral characterization of microcrystals of an organic semiconductor, TIPS-pentacene (6,13-bis-(triisopropylsilylethynyl)pentacene, TIPS-Pn), which undergoes exothermic singlet fission on a \sim 100 fs time scale.^{20,27} We correlate the local morphology of individual TIPS-Pn microstructures determined using AFM topographic mapping with broadband TA imaging to measure the spatial variation of the spectral response within individual microcrystals. Targeted high-resolution 2DWL measurements are then used to further characterize heterogeneity at specific locations within single microcrystals. Thus, by combining an AFM, TA microscope, and 2DWL spectrometer, we demonstrate a characterization

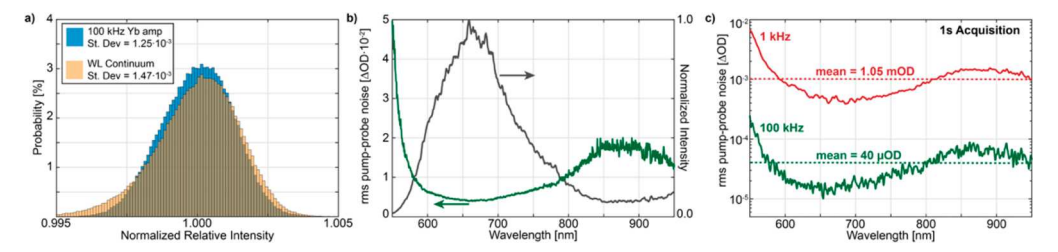


Figure 2. (a) Relative intensity noise comparison of the fundamental ($\lambda = 1040$ nm) and spectrally integrated WL supercontinuum for $\sim 10^6$ sequential laser shots. (b) Spectral distribution of the rms noise in the measured optical density for sequential laser shots (green) and spectrum of WL supercontinuum (black). (c) Distribution of the total rms noise, corresponding to a 1 s acquisition, shown for repetition rates of 100 and 1 kHz, respectively.

technique which can first identify and topographically characterize individual nanostructures using AFM, and subsequently spatially and spectrally map the nanostructure's intrinsic ultrafast response using TA imaging and high-resolution 2DES.

2. EXPERIMENTAL METHODS

Multidimensional spectra can be measured in a variety of geometries, but the optical alignment of multiple pump and probe pulses into a single microscope objective can be facilitated by implementation of a colinear beam geometry. 10,30-33 The process of measuring a multidimensional spectrum is performed here using a high-repetition rate, broadband AOM pulse shaping system based on our previously reported 2DWL spectroscopy system.⁶ The WL generation, shaping of the spectral phase, and focusing optics necessary for 2DWL microscopy measurements are pictured in Figure 1. While broad bandwidth pulses have been achieved from NOPA¹¹⁻¹⁴ and hollow-core fiber light sources,⁷⁻¹⁰ we generate WL supercontinuum via filamentation in a solidstate material to directly act as a light source for both the pump and probe pulses.⁵ Using an amplified, subps, Yb laser as a light source, the resulting supercontinuum is coherent³⁴ and can spectrally range from ~500 to 1600 nm when using YAG as a filamentation medium.^{35,36} The total pulse energy associated with WL continua (~nanojoules) is orders of magnitude weaker than amplified ultrafast visible light sources, however, the reduced focal volumes results in pump-probe signal strengths that are sufficient for many materials and biological samples.^{6,37} Further tight focusing using a microscope objective allows for pump fluences of up to $\sim 250 \ \mu \text{J/cm}^2$ in the sample focus, which often necessitates attenuation of the pulses to prevent damage or sample degradation.

To generate WL supercontinuum for this experiment, we use a Yb:KYW amplifier (Spirit, Spectra Physics) with a center wavelength of $\lambda = 1040$ nm, pulse duration of ~400 fs, and pulse energy of $\sim 10 \mu J$. These pulses are divided equally between pump and probe arms and directed through a WL generation system consisting of a waveplate/polarizer variable attenuator, focusing lens (f = 75 mm) and a YAG crystal (8 mm and 4 mm for the pump and probe, respectively) to produce a stable supercontinuum spectrum. The probe-arm of the experiment contains an additional optical chopper which selectively transmits every other pulse allowing for further discrimination of signals related to pump-scatter (see discussion below). The broadband spectral distribution of the pump and probe pulses are displayed in Figure 1c. While the source of the pump and probe pulses are both generated via WL filamentation, the spectral distribution of the pump at

the sample varies slightly due to the relative efficiency of the gratings within the 4-f AOM pulse-shaper.

To minimize measurement time for imaging applications, it is important to collect data as quickly as possible. In order to achieve a desired signal-to-noise with a minimal acquisition time, we implement a high repetition rate amplifier system operating at 100 kHz to both maximize the rate of signal acquisition and minimize the intensity fluctuations between sequential pulses as a means of lowering the noise floor of the measurement. Owing to a longer excited state lifetime, utilizing amplified pulses from a Yb-based system at higher (>100 kHz) repetition rates allows for a reduction of shot-to-shot energy fluctuations with respect to kHz based Ti:sapph amplifier systems. For the laser system used here (Spirit 4W Yb:KYW), pulse energy fluctuations of the fundamental laser of ~0.125% rms were observed (Figure 2a). Through optimization of the focal conditions for WL filamentation, corresponding energy fluctuations of $\sim 0.15\%$ were observed for the supercontinuum. This noise is only fractionally higher than the fundamental laser noise emphasizing that a combination of low laser-noise, high mechanical stability, and rapid acquisition can be used to minimize the noise floor of TA and 2DWL measurements. To determine the noise-floor of a pump-probe measurement, we measured the average normalized intensity difference between sequential laser shots. Here, the spectral variation of rms noise associated with the change in optical density is inversely related to the root of the spectral intensity, $\propto S(\omega)^{-1/2}$, of the WL distribution as pictured in Figure 2b. Further, by increasing the acquisition rate, we observe that the measured signal-to-noise ratio improves faster than would be expected from increasing the number of collected data points alone. This increase is attributable to higher coherence between neighboring laser shots at high repetition rates.^{6,38} In this case, the reduction of the noise floor for pump-probe measurements can be demonstrated through the comparison of the noise-floor for a 1 s acquisition at laser repetition rates of 1 kHz and 100 kHz. While a factor of 10 decrease would be expected from the increased sampling alone, we observe a decrease by a factor of \sim 25.

Temporal pulse compression of both the pump and probe pulses is achieved using a combination of dispersion compensation techniques. For the probe pulse, which passes through a minimal amount of transmissive material, dispersion compensation of both group delay dispersion (GDD) and third-order dispersion (TOD) is achieved via a broadband chirped-mirror compressor (Layertech GmbH, #132580). Thirteen bounce-pairs compensate for $\sim 570 \text{ fs}^2$ of GDD and $\sim 300 \text{ fs}^3$ of TOD compensating for the 4 mm YAG supercontinuum generation crystal and 2 mm of SiO₂ in the

probe beampath. For the pump pulse sequence generated by the AOM pulse-shaper system, temporal compression involves a number of components, both active and passive. These elements include a chirped-mirror precompressor, a static dispersion contribution resulting from the AOM-grating geometry, and the actively controlled spectral phase shaping provided by the AOM itself. The complete dispersion balancing of the TeO2 based AOM system is detailed in the next section.

Following dispersion compensation and pulse-shaping to generate a temporally compressed 2DWL-pulse sequence, the pump and probe pulses are combined in a cross-polarized relationship using a broadband thin-film polarizer and directed through a bottom illumination reflective focusing objective $(50 \times, NA = 0.65)$. Light transmitted by the sample is collected by an $(20 \times, NA = 0.6)$ objective, polarization filtered to isolate the transmitted probe pulse, and fiber coupled for detection using a synchronized spectrometer, also operating at 100 kHz (SpectraPro2150, Princeton Instruments, e2V AviivA EM4). While the spatial-resolution of TA and 2DWL measurements are primarily governed by the third-order processes which generate signal, the process of fiber coupling the transmitted light from the collection objectives additionally acts as a pinhole enabling the system to further act as a confocal microscope for linear spectroscopic measurements as well.

One particular advantage of AOM based pulse-shaping systems is that the spectral phase and amplitude used to increment the time-delay and relative phase of the pump pulse sequence can be modulated on a shot-to-shot basis at repetition rates up to ~300 kHz. The rate of 100 kHz used here corresponds to the limiting readout rate of the synchronized detector. As stated above, data acquisition at high repetition rates is doubly advantageous, first by virtue of an increased rate of data collection, and second due to the reduced relative noise between sequential measurements. 6,38 As illustrated by the relative pump-probe measurement noise in Figure 2c, high-repetition rate shot-to-shot detection allows for minimization of the effects of low frequency noise in the light source by reducing contributions from slow power drifts, 1/f noise, and electronic noise.

A typical 2DWL measurement is performed by measuring the transient absorption spectrum of the probe pulse corresponding to an increasing series of coherence times of the pump-pulse pair. Phase cycling of the relative phase of a pump-pulse pair (φ_1, φ_2) with respect to one another is implemented to reduce the effect of pump-scatter interference with the detected probe. The probe pulse is further modulated on/off at 50 kHz with an AOM chopper as a means of subtracting any residual leak-through of the pump following polarization filtering prior to detection with a synchronized spectrometer. The result is an 8-frame pulse sequence for each coherence time in the 2DWL measurement (four pump-pulse phase relationships: $[(\varphi_1 = 0, \varphi_2 = 0), (\varphi_1 = 0, \varphi_2 = \pi), (\varphi_1 = 0, \varphi_2 = \pi)]$ π , $\varphi_2 = 0$), $(\varphi_1 = \pi, \varphi_2 = \pi)$] each combined with a two-pulse probe sequence (probe-on/probe-off)). A typical 2DWL measurement consists of a sequence of 400 pump-pulse combinations corresponding to a set of 50 coherence time delays, each with its own 8-frame pump/probe phase sequence, which results in a total acquisition time for a single spectrum of 4 ms. The measurement of this 2DWL sequence can then be repeated until the desired signal-to-noise ratio is achieved.

3. BROADBAND DISPERSION COMPENSATION **USING AOM PULSE-SHAPING**

In order to perform time-resolved spectroscopy experiments, it is essential that the temporal duration of the pump and probe pulses are minimized. This requirement represents a significant challenge for broadband spectroscopies in the visible spectral range, as transmissive materials in the beampath can incur significant dispersive chirping of the optical pulse. Due to its high dispersion (GDD[675 nm] = $660 \text{ fs}^2/\text{mm}$), implementation of a TeO2-based AOM for pulse-shaping across a broad spectral range requires precise balancing of the dispersion contributions within the optical beampath. Interestingly, we found that the net external dispersion compensation necessary to temporally compress the WL supercontinua for the pump pulse sequence was much less than expected given the large dispersion and optical path length within the TeO2 based AOM pulse-shaper. As detailed in the following section, this discrepancy is the result of an additional dispersive contribution stemming from the geometric parameters of the 4-f shaper and the scaling relationship between the optical frequencies of the WL pulse with the phase of the acoustic waveform within the AOM.

In general, control over the temporal profile of the pulse sequence is performed via dispersion compensation of the spectral phase. Here, the relation of the electric field, E, of a given optical pulse with the spectral phase may be expressed as $E(\omega) = \sqrt{S(\omega)} \cdot e^{-i\psi(\omega)}$, where $S(\omega) = |E(\omega)|^2$ represents the spectral intensity and $\psi(\omega)$ represents the spectral phase of the pulse. Expressing $\psi(\omega)$ as a Taylor series, the spectral phase may be described using terms associated with the linear groupdelay (ψ_1, GD) , second order group-delay dispersion (ψ_2, GD) GDD), third order (ψ_3 , TOD), fourth order (ψ_4 , FOD), ...to *n*th order dispersion, $\psi_n = \frac{\partial^n \psi}{\partial \omega^n}$.

$$\psi(\omega) = \psi(\omega_0) + \frac{\partial \psi(\omega_0)}{\partial \omega} (\omega - \omega_0) + \frac{1}{2} \frac{\partial^2 \psi(\omega_0)}{\partial \omega^2} (\omega - \omega_0)^2 + \dots$$

$$= \psi_0 + \psi_1 \cdot (\omega - \omega_0) + \frac{\psi_2}{2} \cdot (\omega - \omega_0)^2 + \dots$$
(1)

The total spectral phase of the 2DWL microscopy system can be viewed as a superposition of contributions representing the phase associated with normal and anomalous dispersive optical elements in addition to the compensatory spectral phase applied by the AOM mask. Normal dispersive optical elements $\psi_{ND}(\omega)$ represent elements with positive dispersion for which the propagation time, $\tau = \frac{\partial \psi}{\partial \omega}$, is positive, $\frac{\partial \tau}{\partial \omega} > 0$. Conversely, anomalously dispersive $\psi_{AD}(\omega)$ elements are those which exhibit negative dispersion, $\frac{\partial \tau}{\partial \omega} < 0$. In order to temporally compress the pump-pulse sequence generated by the AOM, a user-defined compensatory spectral phase mask $\psi_M(\omega)$ is applied using the AOM. Here, $\psi_M(\omega)$ serves a variety of purposes including application of a controlled phase offset, the use of phase-modulation as a means of generating multiple pulses, and employing a spectral phase offset to precisely balance the net group-delay of the entire 2DWL microscopy system at the sample focus.

Implementation of a pulse-shaper for the 2DWL microscopy measurements not only enables dispersion compensation as a means of temporally compressing the optical pulse but also allows for the generation of a colinear pump-pulse pair with a user defined relative-phase offset and coherence time

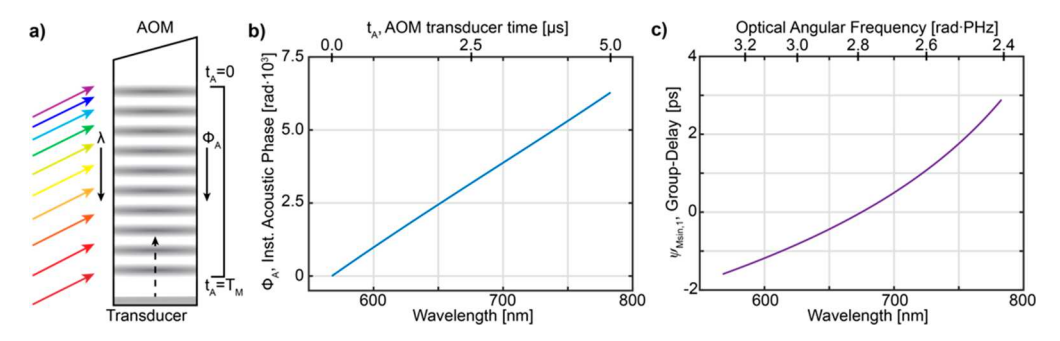


Figure 3. (a) Schematic of the AOM geometry illustrating (b) the linear scaling of the optical wavelength and the instantaneous phase of the AOM sinusoidal wave for the TeO2 AOM described in the main text. Using this instantaneous phase, the (c) group-delay relative to the center wavelength of $\lambda = 675$ nm can be determined using chain-rule differentiation for -1 order diffraction, $\frac{d\psi}{d\omega} = -\frac{d\Phi_A}{dr_A}\frac{dr_A}{d\omega}$

separation. Here, the application of a custom spectral amplitude and phase mask, M, may be expressed in frequency space as

$$E'(\omega) = M(\omega) \cdot E(\omega) = |M(\omega)| E(\omega) \cdot e^{-i\psi_M(\omega)}$$
 (2)

where $E(\omega)$ represents the electric field of the incoming optical pulse, and $E'(\omega)$ the outgoing shaped electric field. For the measurement of multidimensional spectra using a pumpprobe geometry, it is commonplace to implement shaping to create a pulse-pair with relative phase-offsets of φ_1 and φ_2 respectively, separated by a coherence time-delay τ_c . This specific AOM mask function, M_{2D} , can be represented using a modified form as^{22,2}

$$M_{2D}(\omega) = \frac{1}{2} \cdot \left(e^{-i\varphi_1} + e^{-i(\omega \tau_c + \varphi_2)} \right) \cdot e^{-i\psi_M(\omega)}$$
(3)

The imposition of $M(\omega)$ on $E(\omega)$ by the AOM physically occurs via diffraction from the periodic modulation of the refractive index of the AOM crystal. 40,41 Depicted in Figure 3a, these modulations are caused by a traveling acoustic wave launched with center frequency f_0 by a transducer over a fixed time-window spanning a range of $t_A = 0$ to T_A with t_A representing the relative time of the AOM transducer output and T_A the duration of the acoustic wave. When light incident upon the AOM is close to the Bragg condition, it may be efficiently diffracted by the acoustic wave into either the +1 or -1 diffraction orders. As a consequence of momentum conservation, the frequency and phase of the diffracted optical beam is shifted by the corresponding frequency and phase of the acoustic wave. For the 4-f AOM shaper implemented here, the incident light travels with a component along the same direction as the acoustic wave resulting in -1 order diffraction and a negative-frequency/phase shift.⁴² The form of this acoustic wave can be generally expressed as

$$\mathcal{A}(t_{\mathbf{A}}) = a(t_{\mathbf{A}}) \cdot \sin(2\pi f_0 t_{\mathbf{A}} + \Psi_{\mathbf{A}}(t_{\mathbf{A}})) \tag{4}$$

where $a(t_A)$ and $\Psi_A(t_A)$ represent the amplitude and phase of the acoustic wave, respectively.²²

The spectral amplitude, $|M(\omega)|$, and phase, $\psi_M(\omega)$, may be mapped to the physical parameters of the acoustic wave, $a(t_A)$ and $\Psi_A(t_A)$, using the relationship between the optical frequency ω and AOM transducer timing t_A . This calibration is performed using a polynomial expansion with c_n terms representing the calibration constants:

$$\omega(t_{\rm A}) = c_0 + c_1 t_{\rm A} + c_2 t_{\rm A}^2 + \dots$$
 (5)

This expansion, in practice quadratic, captures the parameters of the 4-f shaper (grating groove density, focal length, AOM position, etc..) as well as the linear scaling of wavelength λ across the acoustic aperture of the AOM waveform. As a result, the relationship between $|M(\omega)|$, $\psi_{M}(\omega)$, and the properties of the acoustic wave can be established via the following relations with the sign determined by the order of diffraction:

$$M(\omega(t_{A})) = a(t_{A})$$

$$\psi_{M}(\omega(t_{A})) = \pm \Psi_{A}(t_{A})$$
(6)

For any given AOM transducer waveform, it is often convenient to express the net phase of the sinusoidal acoustic waveform in terms of the instantaneous phase parameter, Φ_A .

$$\Phi_{\mathbf{A}}(t_{\mathbf{A}}) = 2\pi f_{\mathbf{0}} t_{\mathbf{A}} + \Psi_{\mathbf{A}}(t_{\mathbf{A}}) \tag{7}$$

The AOM transducer frequency required to implement this phase shift is characterized by a corresponding instantaneous frequency, $\nu_{\rm A.~in}$:²²

$$\nu_{\rm A,in}(t_{\rm A}) = \frac{\mathrm{d}\Phi_{\rm A}}{\mathrm{d}t_{\rm A}} = 2\pi f_0 + \frac{\mathrm{d}\Psi_{\rm A}(t_{\rm A})}{\mathrm{d}t_{\rm A}} \tag{8}$$

In utilizing the AOM pulse-shaping system to apply dispersion compensation, the primary objective is to apply an active spectral phase-compensation mask which minimizes the group-delay across the spectral range of the pump-pulse. This condition is met when the derivative of the net spectral phase of the entire system, $\frac{\partial \psi_{net}(\omega)}{\partial \omega} - \frac{\partial \psi_{net}(\omega_0)}{\partial \omega} \cong 0$, is zero. Here, ψ_{net} exists as a superposition of ψ_{ND} , ψ_{AD} , the user-defined spectral phase compensation (ψ_M) , and a final spectral-phase contribution $(\psi_{M,\sin})$ associated with the sinusoidal wave of the AOM itself.

$$\psi_{net}(\omega) = \psi_{ND}(\omega) + \psi_{AD}(\omega) + \psi_{M,\sin}(\omega) + \psi_{M}(\omega)$$
 (9)

 ψ_{ND} specifically corresponds to normal dispersive optical elements, i.e., most transmissive optical materials in the visible spectral range. This term includes the spectral phase contribution associated with transmission through the AOM, which itself can be highly dispersive. In contrast to normal dispersion, the ψ_{AD} term represents optical elements providing anomalous dispersion. While this term can correspond to a variety of optical systems such as prism or grating compressors, for our microscopy apparatus it corresponds to the broadband negatively chirped-mirror compressor implemented prior to the AOM pulse-shaper.

The final two terms in eq 9 represent the net spectral phase applied via the AOM pulse shaping system, ϕ_M , which can be written in terms of the instantaneous phase of the AOM transducer output, $\phi_M(\omega) = \psi_{M,\sin}(\omega) + \psi_M(\omega) = \pm \Phi_A(t_A(\omega))$ with the sign determined by the order of diffraction. This relationship directly links the spectral phase contribution associated with the AOM mask with the physical characteristics of the AOM waveform contained in eq 6:

$$\psi_{M,\sin}(\omega(t_{A})) = \pm 2\pi f_{0} t_{A}$$

$$\psi_{M}(\omega(t_{A})) = \pm \Psi_{A}(t_{A})$$
(10)

The source of the spectral phase contribution associated with $\psi_{M,\sin}$ stems from the distribution of optical frequencies across the acoustic aperture of the AOM, specifically the linear component of the instantaneous phase, $2\pi f_0 t_A$. eq 5 indicates that the relationship between ω and t_A includes high-order terms. As depicted in parts b and c of Figure 3, re-expressing $\psi_{M,\sin}$ as a function of ω is thus a nonlinear relationship implying that higher-order spectral phase contributions ($\psi_{M\sin,n} = \frac{\mathrm{d}^n \psi_{M,\sin}}{\mathrm{d}\omega^n} \neq 0$) associated with the sinusoidal acoustic wave must be present. The magnitude of these contributions can be determined by expressing the first term in eq 7 as a function of ω . Here, the linear component of the instantaneous phase associated with a sinusoidal acoustic wave with frequency, f_0 , can be written in terms of a Taylor expansion surrounding the central optical angular frequency, ω_0 .

$$2\pi f_0 t_{\rm A}(\omega) = \psi_{\rm Msin,0} + \psi_{\rm Msin,1}(\omega - \omega_0) + \frac{\psi_{\rm Msin,2}}{2} (\omega - \omega_0)^2 + \frac{\psi_{\rm Msin,3}}{6} (\omega - \omega_0)^3 + \frac{\psi_{\rm Msin,4}}{24} (\omega - \omega_0)^4 ...$$
(11)

Finally, ψ_M represents the component of the dispersion, which is readily adjustable by the user. It is instructive to first estimate the achievable magnitude of spectral phase compensation, which the AOM is capable of producing. Experimentally, the range of spectral phase compensation is limited by the bandwidth of frequencies the AOM transducer is able to generate. Using eq 7 and 8 to relate spectral phase mask to the instantaneous phase, a first order estimate of the maximum possible second order spectral phase compensation $\psi_M(\omega) = \frac{\psi_2}{2}(\omega - \omega_0)^2$ achievable using the AOM may be derived. Here, for an acoustic wave with duration, T_M , whose acoustic aperture spans an optical frequency range, $\Delta\omega = \omega(T_M) - \omega(0)$, the necessary acoustic bandwidth, Δf_{AOM} , needed to provide a second order spectral phase offset ψ_2 can be approximated as

$$\Delta f_{\text{AOM}} = \frac{1}{2\pi} |\nu_{\text{A,inst}}(T_{\text{M}}) - \nu_{\text{A,inst}}(0)|$$

$$= \left| \frac{d\Phi_{\text{A}}(T_{\text{M}})}{dt_{\text{A}}} - \frac{d\Phi_{\text{A}}(0)}{dt_{\text{A}}} \right| = \left| \frac{\psi_{2} \cdot \Delta \omega}{2\pi} \frac{d\omega(t_{\text{A}})}{dt_{\text{A}}} \right|$$

$$\approx \left| \frac{\psi_{2} \cdot \Delta \omega^{2}}{2\pi \cdot T_{\text{M}}} \right|$$
(12)

The quadratic scaling of $\Delta f_{\rm AOM}$ with respect to the optical bandwidth of the pump, $\Delta \omega$, in eq 12 underscores the challenge of providing dispersion compensation for broadbandwidth applications. For example, the TeO₂ AOM used in

this study operates with a center frequency of $f_0 = 200$ MHz and a maximum bandwidth of $\Delta f_{AOM} = 100$ MHz to generate an acoustic mask of duration $T_{\rm M} = 5~\mu {\rm s}$ with an aperture covering wavelengths ranging from 570 to 780 nm ($\Delta \omega \cong 0.9~{\rm rad \cdot PHz}$). The resulting limit for GDD compensation by the AOM is ~3900 fs². This constraint creates a problem for temporal pulse compression as the GDD of the TeO₂ AOM, with a thickness of $L = 10~{\rm mm}$, is ~6600 fs² at the center wavelength of 675 nm. Thus, for the large spectral bandwidth of the pump, $\psi_{M}(\omega)$ alone cannot even compensate for the normal dispersion associated with transmission through the AOM crystal.

With this challenge in mind, the intrinsic dispersion associated with the sinusoidal wave $\psi_{M,\sin}(\omega)$ allows for additional spectral phase compensation as a means of balancing the group-delay of the entire system. Here, the dispersion parameters, $\psi_{M\sin,n}$, describe the orders (GD, GDD, TOD, ...) of the spectral phase associated with a pure sinusoidal AOM acoustic wave characterized by an instantaneous phase of $\Phi_A(t_A) = 2\pi f_0 t_A$. As an illustration, the geometric parameters of the 4-f TeO2 AOM used here result in the following calibration constants: $c_0 \cong 3.32 \text{ rad-PHz}$, $c_1 \cong -2.36 \times 10^5 \text{rad} \cdot \frac{\text{PHz}}{\text{s}}$, and $c_2 \cong 1.08 \times 10^{10} \text{rad} \cdot \frac{\text{PHz}}{\text{s}^2}$, capturing the mapping of lower optical frequencies to longer transducer time-delays in the AOM acoustic waveform. Performing the expansion in eq 11 with these calibration parameters shows that the net spectral phase contribution of the sinusoidal wave corresponds to dispersive parameters of $\psi_{M\sin,2} = -4560 \text{ fs}^2$, $\psi_{M\sin,3} = 10270 \text{ fs}^3$, and $\psi_{M\sin,4} = -27600$ fs⁴. The magnitude of these dispersion parameters is substantial, surpassing the compensation range of the AOM itself. Most importantly, the combined GDD contributions of the AOM mask, $\psi_{M,2}$ + $\psi_{M\sin,2}$, are now capable of compensating for the normal material dispersion of the AOM itself.

It is interesting to note that by switching whether optical frequencies map from blue to red onto the time delay of the acoustic waveform or vice versa, one can reverse the signs of the dispersion terms associated with $\psi_{M, \sin}$. In order to achieve a balanced dispersion for the experiment with a residual spectral phase contribution within the compensation range of ψ_M , it is thus essential to select the geometric orientation of the 4-f pulse-shaper in a manner which results in a $\psi_{M, \sin}$ which acts to offset the normal dispersion of the AOM.

Table 1 displays the dispersion terms associated with the TeO_2 AOM used here and the associated transmissive optics in the 2DWL microscopy system. The net dispersion is balanced via a combination of active and passive dispersion compensation along with the geometric parameters of the pulse shaper. The corresponding net group-delay associated with each of the various elements of the pump beam path for

Table 1. Spectral Phase Parameters ($\lambda_0 = 675 \text{ nm}$) Associated with TeO₂ AOM-Based 2DWL Microscopy System

Phase Term	GDD (fs ²)	TOD (fs^3)	FOD (fs ⁴)
ψ_{ND}	6600 + (1460)	4290 + (690)	2990 + (-10)
ψ_{AD}	-1760	0	0
ψ_M	-1650	-15250	24620
$\psi_{M, ext{sin}}$	-4650	10270	-27600
ψ_{Net}	0	0	0

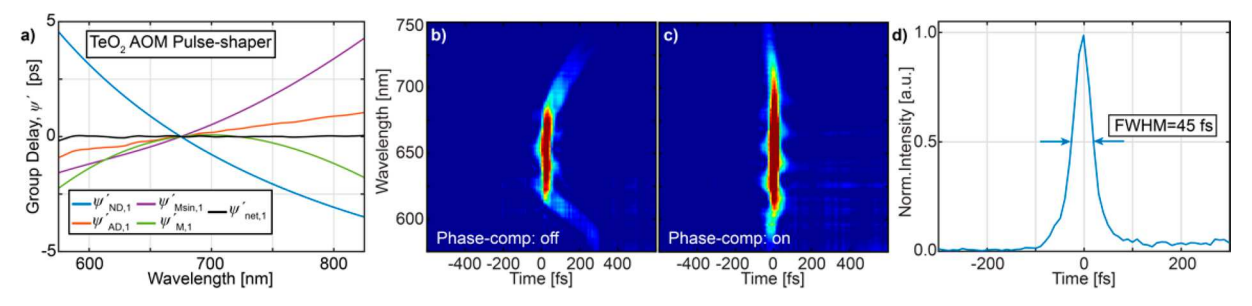


Figure 4. (a) Graphical representation of the net group delay $(\psi'_{\text{net},l})$ of the pump optical beam-path with respect to group delay of normal dispersion $(\psi'_{ND,1})$, anomalous dispersion (ψ'_{AD}) , the static dispersion associated with the sinusoidal AOM waveform $(\psi'_{Msin,1})$, and the active dispersion compensation applied by the AOM $(y'_{M,1})$ with respect to a central wavelength of $\lambda = 675$ nm. (b, c) Polarization-gating FROG characterization of the pump pulse without and with active pulse compensation from the AOM pulse-shaper, respectively. (d) Integrated spectral intensity of the pump pulse exhibiting a <50 fs fwhm.

the TeO₂ AOM is shown in Figure 4. Here, ψ_{ND} is determined by the optical thickness of the AOM ($L_{AOM} = 10 \text{ mm}$) and the other transmissive optical elements in the pump beampath $(L_{YAG} = 8 \text{ mm and } L_{SiO_2} = 11 \text{ mm})$ which are contained by the term in parentheses. ψ_{AD} is generated via the ~44 bounces on a negative chirped mirror compressor system. ψ_M and $\psi_{M,\sin}$ represent the user defined and static sinusoidal spectral phase contributions associated with the application of the AOM phase mask with ψ_{Net} representing the net dispersion of the complete 2DWL microscopy system.

As shown in Figure 4a, these dispersion contributions can be chosen to precisely balance one another yielding a net group delay of zero across the entire bandwidth of the pump pulse. The negative dispersive effect of $\psi_{M, \sin}$ can clearly be visualized as the most significant contribution of negative GDD, without which full temporal compression of the pump-pulse would not be possible. Careful selection of dispersion contributions, both active and passive, is thus critical in achieve full temporal compression of the pulses.

The specific effect of the active phase compensation provided by the AOM pulse-shaper is depicted via the polarization-gating frequency resolved optical gating (PG-FROG) measurements (Figure 4b,c) using the <30 fs output of a NOPA as an optical gate in a crossed-beam geometry; the duration of the probe pulse was similarly measured to confirm its temporal compression. 43 These measurements were performed at a separate sample location than the 2DWL microscope system but with an optical beampath in which all dispersive element were shared. PG-FROG traces of the pumpbeam demonstrate the impact of the AOM spectral phase mask by characterizing the temporal profile of the pulse before and after the active phase compensation, ψ_M , has been turned on. Here, the user-controlled spectral phase compensation mask enables for compression of the WL supercontinua down to a pulse-durations of <50 fs (Figure 4d). Notably, the utility of the pulse shaper does not simply lie in precise temporal compression of the pump pulse, but also in the ability to produce the user-defined pump-pulse sequences necessary for acquiring 2DWL spectra. As demonstrated in the following section, the ability to generate a pair of pump-pulses with welldefined temporal separation and relative phase on a shot-toshot basis enables the acquisition of 2DWL spectra on ~millisecond time scales. It is the combination of these fast acquisition techniques with confocal microscopy which enables the acquisition of multidimensional spectra with simultaneous broad-spectral bandwidth and high temporal/spatial resolu-

4. DEMONSTRATION OF BROADBAND 2DWL MICROSCOPY ON A SINGLET FISSION MATERIAL

The process of singlet fission has long been of research interest as the prospect of carrier multiplication provides a promising means for increasing the efficiency of photovoltaic devices beyond the Shockley-Queisser limit. 44,45 Here, singlet fission represents a mechanism by which a singlet exciton formed by the absorption of a single photon undergoes a spin-allowed transition into two triplet excitons. One particular class of materials who have been shown to exhibit singlet fission are polyacenes. For these materials the geometric relationships between neighboring molecules is known to play a critical role in determining the intermolecular couplings which govern the energetics and kinetics of the singlet fission process.^{46–50}

The role of intermolecular coupling in singlet fission motivates the study of links between local sample morphology and energy transfer pathways, as morphology determines the couplings between molecular chromophores. Understanding these links is of particular importance for the development of more efficient photovoltaic devices. The kinetics of a variety of singlet fission systems have been investigated including single crystals, 16,17,51-54 nanoscale molecular aggregates, 52,55,56 and polycrystalline/disordered thin films, 54,57-60 among others. Despite extensive singlet fission research, studies mapping the correlation between local morphology and the resulting energy transfer pathways remain underdeveloped. Characterization of the spatial distribution and variation of available energy eigenstates and their couplings holds promise in determining where excitations occur, how they diffuse to sites which promote singlet fission, and whether the resulting triplet states are capable of producing useable photocarriers or whether they recombine at low-energy trap sites.

The merging of microscopic methods with broadband TA and 2DWL characterization addresses these needs by enabling spatial imaging of the spectral response of individual microstructures and measurement of how energy transfer pathways vary with sample morphology. These capabilities are of particular interest for photovoltaic materials which often contain multiple electronic absorption features spanning a broad energy range. By measurement with both a broadband pump and probe, it is possible to simultaneously characterize the electronic couplings, ultrafast dynamics, and energy transfer processes that occur among multiple energy eigenstates. Acting in concert with the spatial resolution provided by the AFM and optical microscope, we are further able to correlate variations in energy transfer and the

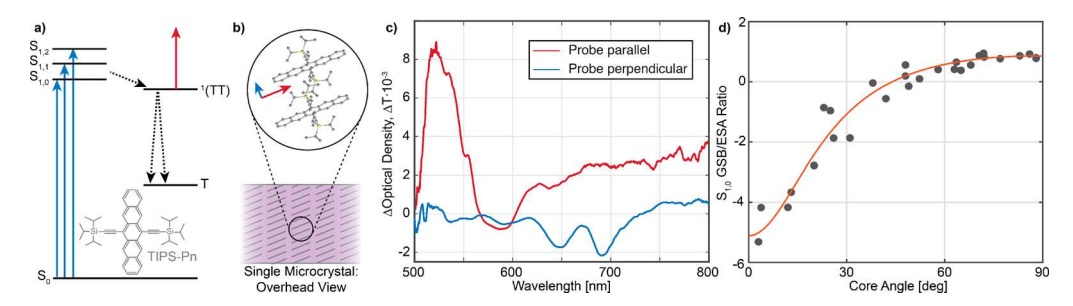


Figure 5. (a) Singlet and triplet state energies in crystalline TIPS-Pn shown with optical transitions associated with S_{1,n} GSB (blue arrows) and ¹(TT) ESA (red arrows). (b) Overhead view of the orientation of TIPS-Pn molecules within an individual microcrystal. Transition dipoles associated with ground state S_{1,n} absorption and ¹(TT) ESA are shown in blue and red respecitively. (c) Spectral distribtion of TA with the probe oriented parallel (red) and perpendicular (blue) to the molecular cores in the microcrystal lattice, respectively. d) relative ratio of GSB signal (λ = 695 nm) to ESA ($\lambda = 750$ nm) as a function of relative crystal angle to the probe polarization for an individual microcyrstal.

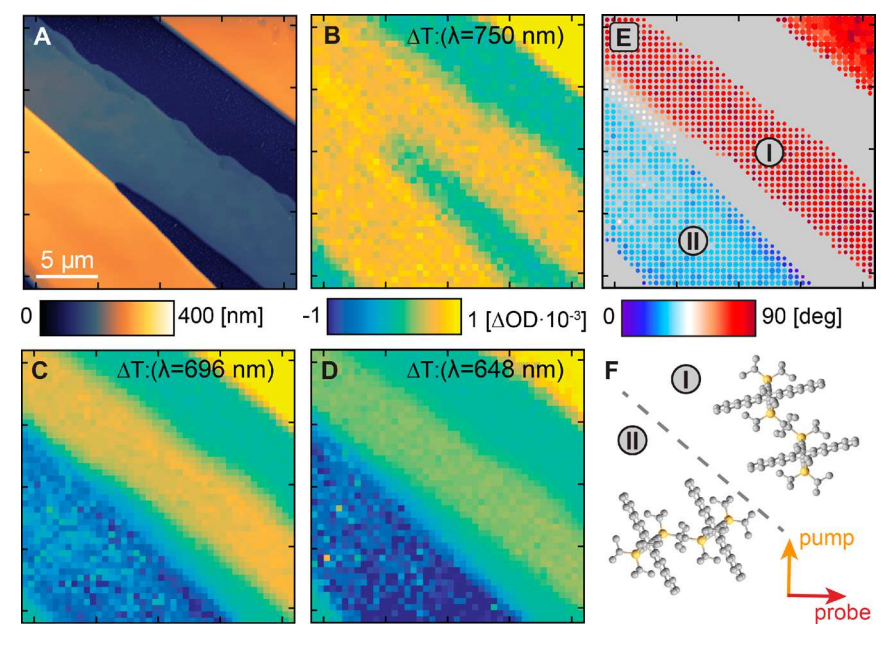


Figure 6. (a) AFM topography of a region containing several TIPS-Pn microcrystals. (b-d) extracted TA images at wavelengths corresponding to ¹(TT) ESA, the S_{1.0} GSB, and the S_{1.1} GSB, respectively. (e) Reconstructed molecular orientation from the GSB/ESA ratio yielding the molecular orientations pictured in part f.

broadband spectral response with specific morphological features in the sample.

As a demonstration we present TA and 2DWL microscopic characterization of microcrystals which exhibit singlet fission on an ultrafast time scale. The specific material we have chosen are thin microcrystals of TIPS-Pn. 61,62 As an organic semiconductor, TIPS-Pn has been of significant research interest because it is both solution processable and exhibits singlet fission. Materials similar to TIPS-Pn have been proposed as potential photosensitizers in solar cells which allow for increases in the total photocurrent achievable from bluer wavelengths such that the internal quantum efficiency can be increased beyond 100%.63-65

Similar to previous studies, the TIPS-Pn microcrystals studied here are fabricated via drop-cast crystallization of a concentrated TIPS-Pn/toluene solution on a glass microscope coverslip in a toluene rich environment. 51-53 The resulting sample consists of a microcrystal distribution which ranges from \sim 100 to 300 nm in thickness, 10-20 μ m in width, and several millimeters in length. Due to the growth conditions as the TIPS-Pn solution dries, neighboring microcrystals are often

locally oriented parallel to one another with the longitudinal axis of the pentacene core parallel to the substrate (Figure 5).⁶⁶

The transient optical response of an individual microcrystal is dependent on the relative orientation of the microcrystal with respect to the pump and probe polarization directions. Initial population of a singlet exciton distribution occurs through excitation of a vibronic progression of singlet states $S_{1,n}$ which spans from 590 to 700 nm. The transition dipole moments of these singlet excitations lie along the short axis of the pentacene cores of the microcrystal (Figure 5b). Following excitation, the singlet population undergoes a rapid (~100 fs) singlet fission process to generate two triplets in a localized correlated triplet-pair state ¹(TT) from which excited state absorption may occur. In contrast to $S_{1,n}$ transitions, the transition dipole moment of the ¹(TT) state lies along the long axis of the pentacene core.

4.1. Characterization of the Orientation Dependence of the Broadband Ultrafast Response. For TA microscopy of TIPS-Pn the transition dipole moments of singlet absorption and triplet excited state absorption are perpendicular to one another. As a result, the magnitude and spectral distribution of

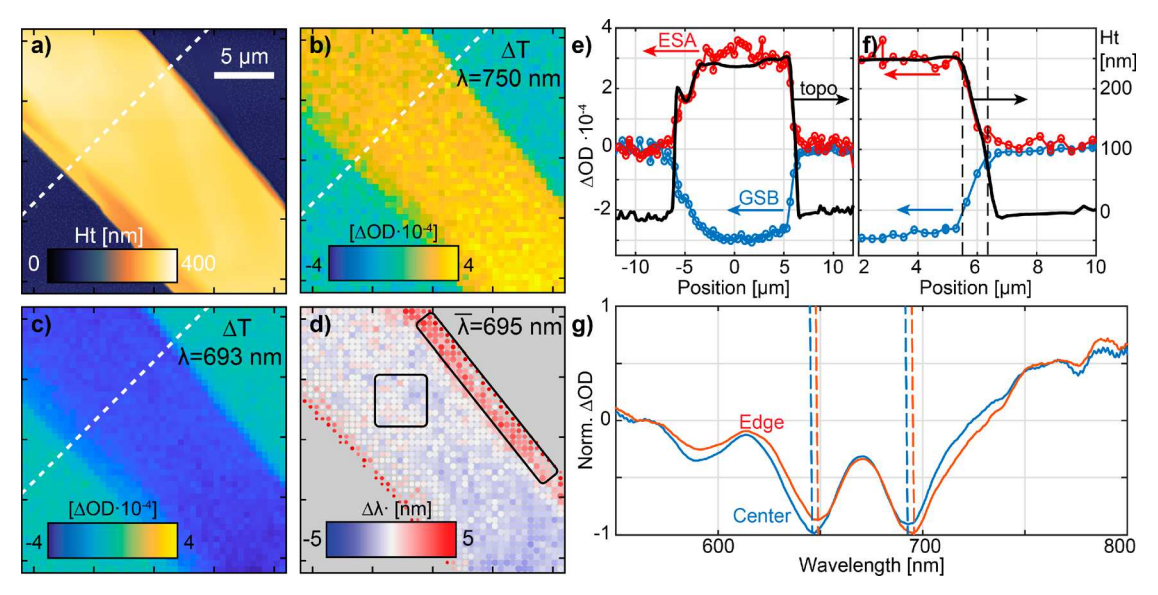


Figure 7. (a) AFM topography of a single TIPS-Pn microcrystal with corresponding TA images at wavelengths associated with the (b) 1 (TT) ESA and the (c) $S_{1,0}$ GSB (T=1 ps). (d) Image depicting the relative shift of the $S_{1,0}$ GSB peak as a function of spatial position indicating that the microcrystal edges are correlated with a spectral redshift of 3–5 nm. (e, f) Cross-sectional lineaut through the microcrystal along the dashed line in panels a–c showing the correlation of AFM topography with the observed ESA at 750 nm and GSB at 669 nm. (g) Variation of the relative peak heights and peak positions of the $S_{1,0}$ and $S_{1,1}$ GSB features displayed through comparison of spectra associated with center and edge regions of the microcrystal. These spectra correspond to the regions indicated in panel d.

the transient response represents a convolution of two factors: the initial pump-excitation of singlets from the ground state, and the subsequent cross-polarized probing of transitions which lie in a perpendicular orientation. Figure 5c displays the spectral distribution measured from a single TIPS-Pn microcrystal in the limiting conditions in which the probe is oriented perpendicular (blue) and parallel (red) with the long-axis of the molecular cores of the microcrystal. Under a perpendicular orientation, while some ESA from the ¹(TT) state is present at longer wavelengths, the probe pulse primarily measures the GSB of the $S_{1,n}$ transitions. Conversely, when the probe is oriented parallel to the long axis of the molecules a strong, broadband ESA is observed associated with the ¹(TT) state. Similar to observations of ESA on pentacene, 44,68 a distinct triplet associated ESA peak emerges near 530 nm while a broadband ESA rises in the NIR for wavelengths greater than 600 nm.

One unique feature of the spectral range of the probe is that it allows for the simultaneous measurement of energy ranges associated with S_{1,n} GSB and ¹(TT) ESA. Comparing the relative ratio of TA signal in spectral ranges associated only with ¹(TT) ESA (i.e., > 750 nm) with those more directly associated with $S_{1,n}$ GSB (i.e., the GSB of the $S_{1,0}$ state at 690 nm) allows for a determination of the relative orientation of an individual microcrystal. Figure 5d displays the variation of the relative ratio of the TA signal at $\lambda = 690$ nm and $\lambda = 750$ nm with respect to the relative angle of the molecular cores of a single microcrystal. The limiting angle of 90 deg is here defined by the maximum relative ratio. On the basis of the projection of the pump and probe onto the crystallographic orientation, an interpolative fit of the relative ratio of the TA signal with respect to the molecular cores within the crystal is further shown. Provided this relationship between the crystal orientation and the relative ratio of the TA signal at differing wavelengths, any individual broadband spectrum can be used

to estimate the relative crystallographic orientation of a particular region or microstructure.

4.2. Broadband TA Imaging via Point-Scanning. By implementing point-by-point raster scanning across a region of interest, full images of the variation of the TA response can be constructed as illustrated in Figure 6. For these measurements, AFM was first utilized to acquire a high resolution (~10 nm) surface image of the sample morphology revealing the presence of three microcrystals with a similar macroscopic orientation. The AFM probe is subsequently withdrawn, and broadband spectra are recorded at correlated locations across the sample to form a TA image.Parts b-d of Figure 6 display the TA response for differing wavelengths corresponding to ¹(TT) ESA, the S_{1.0} GSB, and the S_{1.1} GSB, respectively. While the AFM topography shows that the microcrystals have a similar macroscopic orientation, the optical response indicates that the molecular orientation within the crystal lattice is not identical. This is apparent from the spatial images as the crystals all exhibit similar ESA response at longer wavelengths (Figure 6b), but at shorter wavelengths corresponding to the $S_{1,0}$ and S_{1,1} transitions the lower microcrystal shows a strong GSB while the upper two crystals exhibit ESA (Figure 6c,d). Using the relationship between the relative orientation of the crystal lattice and the GSB/ESA ratio established in Figure 5c, for each pixel of the TA image we can derive an estimate of the crystallographic orientation with respect to the pump and probe polarizations. This mapping is displayed in Figure 6e and shows that the two crystals in the center of the image have two differing crystal orientations as depicted by regions I and II

4.3. Spatial Resolution and Correspondence with AFM-Topography. The diffraction limit and the M^2 parameter of the beam profile are typically defined in terms of a monochromatic wavelength, making definition of the spatial resolution of the four-wave mixing (FWM) process generating the TA signal more nuanced. For four-wave mixing

processes such as TA and 2DES, the signal scales linearly with the pump and probe intensities. In a confocal imaging application in which the pinhole is large compared to the Airy disc, the spatial resolution can be defined in terms of a spatial point spread function (PSF) as $H(r,z) \sim I^2(r,z)$, where I(r,z) represents the intensity distribution. ^{4,30} For the 2DWL microscopy measurements presented here, the broadband pump and probe each have a unique spectral distribution (Figure 1c). This nondegeneracy implies that the PSF for the FWM signal with a given pump/probe wavelength combination must be a function of both the pump λ_p and probe λ_{pr} wavelengths: $H(\lambda_p, \lambda_{pr}, r, z) \sim I(\lambda_p, r, z) \cdot I(\lambda_{pr}, r, z)$. In extending 2DWL microscopy measurements to large bandwidths, it is necessary to consider wavelength scaling effects on the resolution. With this in mind, for the NA and pump wavelengths used here, one would expect the ideal Rayleigh resolution to vary by approximately ±20% from that of the center wavelength.

In lieu of a direct mapping of the wavelength-dependent PSF, the intensity distribution of the spectrally integrated pump and probe can be measured at the sample surface by the AFM probe. Here, with the AFM probe in contact with the surface, the focus of the objective is raster scanned parallel with the surface plane. Using a similar detection mechanism as photothermal IR characterization, 69 by monitoring the component of the AFM tip deflection with a lock-in detector operating at the laser repetition rate, the tip deflection associated with thermal expansion of the surface due to absorption of the laser pulse can be transduced. Figure 1b displays such a mapping of the intensity distribution indicating a fwhm of the focal region of $\sim 1 \mu m$. This expected resolution is confirmed in practice through observation of the signal change over sharp topographical features. Figure 7 illustrates such a change observed for a line trace across the edge of the single microcrystal. The zoom-in to the upper crystal edge region (Figure 7f) shows that the rise of both the GSB at λ = 695 nm and the ESA at $\lambda = 750$ nm occurs over distances slightly less than 1 μ m. While the edge of the microcrystal is not sharp enough to act as a direct measurement of the resolution the absence of TA signal contributions beyond the crystal edge, in addition to the mapping of the intensity distribution of the focus (Figure 1b), indicates that the resolution of the measurement is indeed $\sim 1 \mu m$.

One particular advantage of the implementation of broadband spectroscopic detection is that slight variations of the spectral response can be observed, analyzed, and correlated with specific topographic features present in the sample morphology. Figure 7d provides one such example of how shifts in the relative magnitude and position of the spectral response can be captured by a broadband measurement. Here, variation of the amplitude (dot size) and center wavelength of the $S_{1,0}$ GSB (dot color) is plotted for every pixel of the TA image in Figure 7c. While the TA response at single wavelengths appears relatively homogeneous, analysis of the broadband spectral response reveals spectral shifts and trends within the microcrystal. Specifically, in moving from the center region of the microcrystal to the edge, a relative height change occurs with spectral weight transferring from the S_{1,0} to the S_{1,1} GSB and a slight red-shift in the vibronic progression simultaneously occurs. These effects as displayed by the normalized spectra in Figure 7g were reproducible across several microcrystals.

4.4. Demonstration of Spatially Resolved 2D-WL Spectroscopy. As compared to the TA signal, visualization over both pump and probe spectral dimensions using multidimensional spectroscopy allows for easier identification of slight variations in the spectral response. In addition, 2DWL visualization allows for the observation of electronic couplings and energy transfer processes via the presence of cross-peaks in the multidimensional spectrum. The 2DWL spectra displayed in Figure 8, measured at both the center and the edge region of

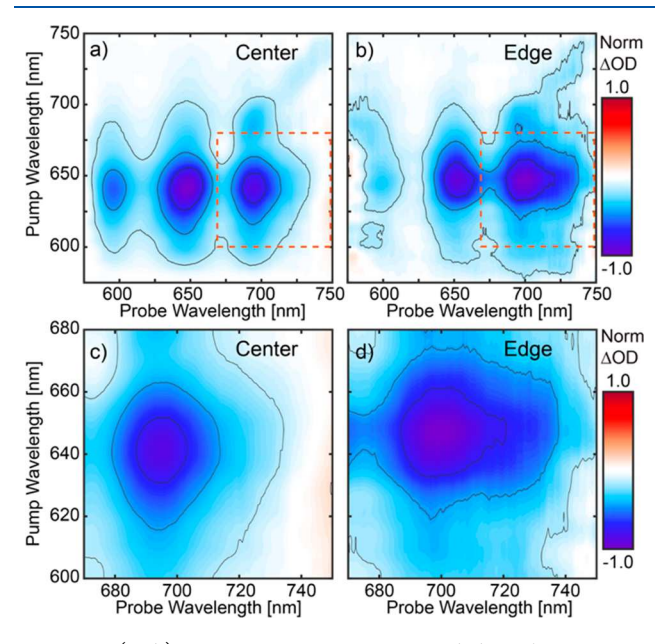


Figure 8. (a, b) 2DWL measurements recorded at the respective center and edge regions of a single microcrystal (T=1 ps). (c, d) Zoom in on the $S_{1,1}/S_{1,0}$ cross-peak region, denoted by the dashed orange box in panels a and b. The cross-peak in this region indicates the emergence of a spectral shoulder for regions near the edge of the microcrystal.

a single microcrystal, provide one such example of how variation of the optical response can be more directly measured. Here, the 2DWL spectra appear primarily as a series of peaks and cross-peaks associated with the $S_{1,0}$ and $S_{1,1}$ GSB.

Comparing the 2DWL spectra at center and edge regions within the region associated with the $S_{1,1}/S_{1,0}$ cross-peak, we note that a clear spectral red-shift and broadening can be observed for 2DWL spectra measured at the microcrystal edge. This increased bleach at longer wavelengths reveals the presence of a higher density of lower energy $S_{1,0}$ states in proximity to the microcrystal edge. The presence of these shallow-energy singlet states correlated with the edge of the microcrystal was reproducible across several microcrystals and has important implications with regard to the energy states and dynamics which govern singlet fission in TIPS-Pn. In general, this type of site specific 2DWL measurement demonstrates how microscopic variation of the energy landscape of a material can be visualized with high resolution and correlated with sample morphology.

5. CONCLUSION

Through a combination of broadband WL generation, AOM-based pulse-shaping, atomic force microscopy, and confocal optical microscopy, we have developed a multimodal 2DWL

microscopy system capable of performing multidimensional spectroscopic measurements with high resolution in temporal, spectral, and spatial dimensions along with hyperspectral TA images. Here, pulse-shaping on a shot-to-shot basis acts to limit the acquisition time of a single 2DWL spectra to a few ms while maximizing the signal-to-noise ratio of the measurement. While implementation of pulse-shaping allows for precision control over the relative timing and phase of an ultrafast pulse sequence, special consideration must be paid to how dispersion compensation is implemented for AOM-based systems operating over a broad spectral bandwidth in order to temporally compress the optical pulse train.

Temporally resolved, broadband confocal microscopy enables the observation of subtle variations within the hyperspectral images associated with spectral shifts or the emergence of weak absorption features that would be imperceptible to narrowband characterization techniques. Our demonstration of the microscopic mapping of the transient spectral response within TIPS-Pn microcrystals illustrates how simultaneous spectral/spatial mapping of the ultrafast properties can yield unique information about the local electronic properties of a material. The observation of a $\sim\!\!5$ nm redshift $S_{1,0}$ absorption peak in correlation with microcrystal edges was specifically made possible because of the broadband spectral distribution available to both the pump and probe pulses.

By performance of further 2DWL microscopic characterization at targeted areas of interest within the microcrystal, the weak signals present within the TA spectral maps were able to be more clearly visualized to reveal the presence of absorption from low-energy singlet states present at the microcrystal edges. Such measurements demonstrate how multidimensional characterization with high resolution may be employed to visualize the relationship between local morphology and electronic couplings/energy transfer processes.

AUTHOR INFORMATION

Corresponding Author

*(M.T.Z.) E-mail: zanni@chem.wisc.edu.

ORCID ®

Andrew C. Jones: 0000-0001-9205-4847 Nicholas M. Kearns: 0000-0003-2059-2800 Martin T. Zanni: 0000-0001-7191-9768

Notes

The authors declare the following competing financial interest(s): M.T.Z. is co-owner of PhaseTech Spectroscopy, Inc., which sells 2D IR/visible spectrometers and pulse shapers.

ACKNOWLEDGMENTS

The authors gratefully acknowledge Chris Middleton for useful discussions regarding the experimental apparatus. This research was supported by the National Science Foundation (NSF CHE 1665110), and the Air Force Office of Scientific Research (FA9550-19-1-0093). M.B.K. is grateful for support from the National Science Foundation Graduate Research Fellowship Program under Grant No. DGE-1747503. Any opinions, findings, and conclusions or recommendations expressed in this material are those of the author(s) and do not necessarily reflect the views of the National Science Foundation.

REFERENCES

- (1) Jonas, D. M. Two-dimensional femtosecond spectroscopy. *Annu. Rev. Phys. Chem.* **2003**, *54* (1), 425–63.
- (2) Fuller, F. D.; Ogilvie, J. P. Experimental implementations of two-dimensional fourier transform electronic spectroscopy. *Annu. Rev. Phys. Chem.* **2015**, *66* (1), *667*–90.
- (3) Smallwood, C. L.; Cundiff, S. T. Multidimensional Coherent Spectroscopy of Semiconductors. *Laser Photonics Rev.* **2018**, *12* (12), 1800171–1800171.
- (4) Davydova, D. y.; de la Cadena, A.; Akimov, D.; Dietzek, B. Transient absorption microscopy: advances in chemical imaging of photoinduced dynamics. *Laser & Photonics Reviews* **2016**, *10* (1), 62–81.
- (5) Mehlenbacher, R. D.; McDonough, T. J.; Grechko, M.; Wu, M. Y.; Arnold, M. S.; Zanni, M. T. Energy transfer pathways in semiconducting carbon nanotubes revealed using two-dimensional white-light spectroscopy. *Nat. Commun.* **2015**, *6*, 6732.
- (6) Kearns, N. M.; Mehlenbacher, R. D.; Jones, A. C.; Zanni, M. T. Broadband 2D electronic spectrometer using white light and pulse shaping: noise and signal evaluation at 1 and 100 kHz. *Opt. Express* **2017**, 25 (7), 7869–7883.
- (7) Ma, X.; Dostal, J.; Brixner, T. Broadband 7-fs diffractive-optic-based 2D electronic spectroscopy using hollow-core fiber compression. *Opt. Express* **2016**, 24 (18), 20781–91.
- (8) Zheng, H.; Caram, J. R.; Dahlberg, P. D.; Rolczynski, B. S.; Viswanathan, S.; Dolzhnikov, D. S.; Khadivi, A.; Talapin, D. V.; Engel, G. S. Dispersion-free continuum two-dimensional electronic spectrometer. *Appl. Opt.* **2014**, *53* (9), 1909–17.
- (9) Son, M.; Mosquera-Vazquez, S.; Schlau-Cohen, G. S. Ultrabroadband 2D electronic spectroscopy with high-speed, shot-to-shot detection. *Opt. Express* **2017**, *25* (16), 18950–18962.
- (10) Seiler, H.; Palato, S.; Kambhampati, P. Coherent multidimensional spectroscopy at optical frequencies in a single beam with optical readout. *J. Chem. Phys.* **2017**, *147* (9), 094203.
- (11) Maiuri, M.; Rehault, J.; Carey, A. M.; Hacking, K.; Garavelli, M.; Lüer, L.; Polli, D.; Cogdell, R. J.; Cerullo, G. Ultra-broadband 2D electronic spectroscopy of carotenoid-bacteriochlorophyll interactions in the LH1 complex of a purple bacterium. *J. Chem. Phys.* **2015**, *142* (21), 212433.
- (12) Jha, A.; Duan, H. G.; Tiwari, V.; Nayak, P. K.; Snaith, H. J.; Thorwart, M.; Miller, R. J. D. Direct observation of ultrafast exciton dissociation in lead iodide perovskite by 2D electronic spectroscopy. *ACS Photonics* **2018**, *5* (3), 852–860.
- (13) Proppe, A. H.; Elkins, M. H.; Voznyy, O.; Pensack, R. D.; Zapata, F.; Besteiro, L. V.; Quan, L. N.; Quintero-Bermudez, R.; Todorovic, P.; Kelley, S. O.; Govorov, A. O.; Gray, S. K.; Infante, I.; Sargent, E. H.; Scholes, G. D. Spectrally resolved ultrafast exciton transfer in mixed Perovskite quantum wells. *J. Phys. Chem. Lett.* **2019**, 10 (3), 419–426.
- (14) Richter, J. M.; Branchi, F.; Valduga de Almeida Camargo, F.; Zhao, B.; Friend, R. H.; Cerullo, G.; Deschler, F. Ultrafast carrier thermalization in lead iodide perovskite probed with two-dimensional electronic spectroscopy. *Nat. Commun.* **2017**, *8* (1), 376.
- (15) Fischer, M. C.; Wilson, J. W.; Robles, F. E.; Warren, W. S. Invited review article: Pump-probe microscopy. *Rev. Sci. Instrum.* **2016**, 87 (3), 031101.
- (16) Zhu, T.; Wan, Y.; Guo, Z.; Johnson, J.; Huang, L. Two birds with one stone: Tailoring singlet fission for both triplet yield and exciton diffusion length. *Adv. Mater.* **2016**, 28 (34), 7539–47.
- (17) Wan, Y.; Guo, Z.; Zhu, T.; Yan, S.; Johnson, J.; Huang, L. Cooperative singlet and triplet exciton transport in tetracene crystals visualized by ultrafast microscopy. *Nat. Chem.* **2015**, *7* (10), 785–92.
- (18) Wang, R.; Ruzicka, B. A.; Kumar, N.; Bellus, M. Z.; Chiu, H.-Y.; Zhao, H. Ultrafast and spatially resolved studies of charge carriers in atomically thin molybdenum disulfide. *Phys. Rev. B: Condens. Matter Mater. Phys.* **2012**, *86* (4), 045406–045406.
- (19) Steves, M. A.; Zheng, H.; Knappenberger, K. L. Correlated spatially resolved two-dimensional electronic and linear absorption spectroscopy. *Opt. Lett.* **2019**, 44 (8), 2117–2117.

- (20) Jones, A. C.; Kearns, N. M.; Ho, J.; Flach, J. T.; Zanni, M. T. Impact of non-equilibrium molecular packings on singlet fission in microcrystals observed using 2D white-light microscopy. *Nat. Chem.* **2019**, DOI: 10.1038/s41557-019-0368-9.
- (21) Myers, J. A.; Lewis, K. L.; Tekavec, P. F.; Ogilvie, J. P. Two-color two-dimensional Fourier transform electronic spectroscopy with a pulse-shaper. *Opt. Express* **2008**, *16* (22), 17420–8.
- (22) Nite, J. M.; Cyran, J. D.; Krummel, A. T. Active Bragg angle compensation for shaping ultrafast mid-infrared pulses. *Opt. Express* **2012**, 20 (21), 23912–20.
- (23) Grumstrup, E. M.; Shim, S.-H.; Montgomery, M. A.; Damrauer, N. H.; Zanni, M. T. Facile collection of two-dimensional electronic spectra using femtosecond pulse-shaping Technology. *Opt. Express* **2007**, *15* (25), 16681–16681.
- (24) Shim, S. H.; Strasfeld, D. B.; Ling, Y. L.; Zanni, M. T. Automated 2D IR spectroscopy using a mid-IR pulse shaper and application of this technology to the human islet amyloid polypeptide. *Proc. Natl. Acad. Sci. U. S. A.* **2007**, 104 (36), 14197–14202.
- (25) Shim, S. H.; Zanni, M. T. How to turn your pump-probe instrument into a multidimensional spectrometer: 2D IR and Vis spectroscopies via pulse shaping. *Phys. Chem. Chem. Phys.* **2009**, *11* (5), 748–61.
- (26) Mehlenbacher, R. D.; Wang, J.; Kearns, N. M.; Shea, M. J.; Flach, J. T.; McDonough, T. J.; Wu, M. Y.; Arnold, M. S.; Zanni, M. T. Ultrafast Exciton Hopping Observed in Bare Semiconducting Carbon Nanotube Thin Films with Two-Dimensional White-Light Spectroscopy. J. Phys. Chem. Lett. 2016, 7 (11), 2024–2031.
- (27) Grieco, C.; Kennehan, E. R.; Rimshaw, A.; Payne, M. M.; Anthony, J. E.; Asbury, J. B. Harnessing Molecular Vibrations to Probe Triplet Dynamics during Singlet Fission. *J. Phys. Chem. Lett.* **2017**, *8* (23), 5700–5706.
- (28) Bakulin, A. A.; Morgan, S. E.; Kehoe, T. B.; Wilson, M. W.; Chin, A. W.; Zigmantas, D.; Egorova, D.; Rao, A. Real-time observation of multiexcitonic states in ultrafast singlet fission using coherent 2D electronic spectroscopy. *Nat. Chem.* **2016**, 8 (1), 16–23.
- (29) Pensack, R. D.; Grieco, C.; Purdum, G. E.; Mazza, S. M.; Tilley, A. J.; Ostroumov, E. E.; Seferos, D. S.; Loo, Y. L.; Asbury, J. B.; Anthony, J. E.; Scholes, G. D. Solution-processable, crystalline material for quantitative singlet fission. *Mater. Horiz.* **2017**, *4* (5), 915–923.
- (30) Tiwari, V.; Matutes, Y. A.; Gardiner, A. T.; Jansen, T. L. C.; Cogdell, R. J.; Ogilvie, J. P. Spatially-resolved fluorescence-detected two-dimensional electronic spectroscopy probes varying excitonic structure in photosynthetic bacteria. *Nat. Commun.* **2018**, *9* (1), 4219.
- (31) Goetz, S.; Li, D.; Kolb, V.; Pflaum, J.; Brixner, T. Coherent two-dimensional fluorescence micro-spectroscopy. *Opt. Express* **2018**, *26* (4), 3915–3915.
- (32) Serrano, A. L.; Ghosh, A.; Ostrander, J. S.; Zanni, M. T. Widefield FTIR microscopy using mid-IR pulse shaping. *Opt. Express* **2015**, 23 (14), 17815–17815.
- (33) Baiz, C. R.; Schach, D.; Tokmakoff, A. Ultrafast 2D IR microscopy. Opt. Express 2014, 22 (15), 18724–18724.
- (34) Bellini, M.; Hansch, T. W. Phase-locked white-light continuum pulses: toward a universal optical frequency-comb synthesizer. *Opt. Lett.* **2000**, 25 (14), 1049–51.
- (35) Bradler, M.; Baum, P.; Riedle, E. Femtosecond continuum generation in bulk laser host materials with sub-µJ pump pulses. *Appl. Phys. B: Lasers Opt.* **2009**, *97* (3), 561–574.
- (36) Calendron, A. L.; Cankaya, H.; Cirmi, G.; Kartner, F. X. Whitelight generation with sub-ps pulses. *Opt. Express* **2015**, 23 (11), 13866–79.
- (37) Mandal, A.; Chen, M.; Foszcz, E. D.; Schultz, J. D.; Kearns, N. M.; Young, R. M.; Zanni, M. T.; Wasielewski, M. R. Two-Dimensional Electronic Spectroscopy Reveals Excitation Energy-Dependent State Mixing during Singlet Fission in a Terrylenediimide Dimer. J. Am. Chem. Soc. 2018, 140 (51), 17907–17914.
- (38) Kanal, F.; Keiber, S.; Eck, R.; Brixner, T. 100-kHz shot-to-shot broadband data acquisition for high-repetition-rate pump—probe spectroscopy. *Opt. Express* **2014**, 22 (14), 16965—16975.

- (39) Weiner, A. M. Ultrafast optical pulse shaping: A tutorial review. *Opt. Commun.* **2011**, 284 (15), 3669–3692.
- (40) Hillegas, C. W.; Tull, J. X.; Goswami, D.; Strickland, D.; Warren, W. S. Femtosecond laser pulse shaping by use of microsecond radio-frequency pulses. *Opt. Lett.* **1994**, *19* (10), 737–737.
- (41) Dugan, M. A.; Tull, J. X.; Warren, W. S. High-resolution acousto-optic shaping of unamplified and amplified femtosecond laser pulses. J. Opt. Soc. Am. B 1997, 14 (9), 2348–2358.
- (42) Li, E.; Yao, J.; Yu, D.; Xi, J.; Chicharo, J. Optical phase shifting with acousto-optic devices. *Opt. Lett.* **2005**, *30* (2), 189–189.
- (43) Trebino, R.; Sweetser, J. N.; Fittinghoff, D. N.; Krumbügel, M. A.; DeLong, K. W.; Kane, D. J.; Richman, B. A. Measuring ultrashort laser pulses in the time-frequency domain using frequency-resolved optical gating. *Rev. Sci. Instrum.* **1997**, *68* (9), 3277–3295.
- (44) Smith, M. B.; Michl, J. Singlet fission. Chem. Rev. 2010, 110 (11), 6891–936.
- (45) Shockley, W.; Queisser, H. J. Detailed Balance Limit of Efficiency of P-N Junction Solar Cells. *J. Appl. Phys.* **1961**, 32 (3), 510–519.
- (46) Pensack, R. D.; Tilley, A. J.; Grieco, C.; Purdum, G. E.; Ostroumov, E. E.; Granger, D. B.; Oblinsky, D. G.; Dean, J. C.; Doucette, G. S.; Asbury, J. B.; Loo, Y.-L.; Seferos, D. S.; Anthony, J. E.; Scholes, G. D. Striking the right balance of intermolecular coupling for high-efficiency singlet fission. *Chemical Science* **2018**, *9* (29), 6240–6259.
- (47) Wang, L.; Olivier, Y.; Prezhdo, O. V.; Beljonne, D. Maximizing singlet fission by intermolecular packing. *J. Phys. Chem. Lett.* **2014**, *5* (19), 3345–3353.
- (48) Nagami, T.; Ito, S.; Kubo, T.; Nakano, M. Intermolecular Packing Effects on Singlet Fission in Oligorylene Dimers. *ACS Omega* **2017**, 2 (8), 5095–5103.
- (49) Bhattacharyya, K.; Datta, A. Polymorphism Controlled Singlet Fission in TIPS-Anthracene: Role of Stacking Orientation. *J. Phys. Chem. C* **2017**, *121* (3), 1412–1420.
- (50) Arias, D. H.; Ryerson, J. L.; Cook, J. D.; Damrauer, N. H.; Johnson, J. C. Polymorphism influences singlet fission rates in tetracene thin films. *Chem. Sci.* **2016**, *7* (2), 1185–1191.
- (51) Wong, C. Y.; Penwell, S. B.; Cotts, B. L.; Noriega, R.; Wu, H.; Ginsberg, N. S. Revealing Exciton Dynamics in a Small-Molecule Organic Semiconducting Film with Subdomain Transient Absorption Microscopy. *J. Phys. Chem. C* **2013**, *117* (42), 22111–22122.
- (52) Wong, C. Y.; Cotts, B. L.; Wu, H.; Ginsberg, N. S. Exciton dynamics reveal aggregates with intermolecular order at hidden interfaces in solution-cast organic semiconducting films. *Nat. Commun.* **2015**, *6*, 5946.
- (53) Folie, B. D.; Haber, J. B.; Refaely-Abramson, S.; Neaton, J. B.; Ginsberg, N. S. Long-Lived Correlated Triplet Pairs in a pi-Stacked Crystalline Pentacene Derivative. *J. Am. Chem. Soc.* **2018**, *140* (6), 2326–2335.
- (54) Piland, G. B.; Bardeen, C. J. How Morphology Affects Singlet Fission in Crystalline Tetracene. *J. Phys. Chem. Lett.* **2015**, *6* (10), 1841–6.
- (55) Tayebjee, M. J. Y.; Schwarz, K. N.; MacQueen, R. W.; Dvorak, M.; Lam, A. W. C.; Ghiggino, K. P.; McCamey, D. R.; Schmidt, T. W.; Conibeer, G. J. Morphological Evolution and Singlet Fission in Aqueous Suspensions of TIPS-Pentacene Nanoparticles. *J. Phys. Chem. C* 2016, 120 (1), 157–165.
- (56) Pensack, R. D.; Tilley, A. J.; Parkin, S. R.; Lee, T. S.; Payne, M. M.; Gao, D.; Jahnke, A. A.; Oblinsky, D. G.; Li, P. F.; Anthony, J. E.; Seferos, D. S.; Scholes, G. D. Exciton delocalization drives rapid singlet fission in nanoparticles of acene derivatives. *J. Am. Chem. Soc.* **2015**, 137 (21), 6790–803.
- (57) Roberts, S. T.; McAnally, R. E.; Mastron, J. N.; Webber, D. H.; Whited, M. T.; Brutchey, R. L.; Thompson, M. E.; Bradforth, S. E. Efficient singlet fission found in a disordered acene film. *J. Am. Chem. Soc.* **2012**, *134*, 6388–6400.
- (58) Schnedermann, C.; Lim, J. M.; Wende, T.; Duarte, A. S.; Ni, L.; Gu, Q.; Sadhanala, A.; Rao, A.; Kukura, P. Sub-10 fs Time-Resolved

- Vibronic Optical Microscopy. J. Phys. Chem. Lett. 2016, 7 (23), 4854–4859.
- (59) Broch, K.; Dieterle, J.; Branchi, F.; Hestand, N. J.; Olivier, Y.; Tamura, H.; Cruz, C.; Nichols, V. M.; Hinderhofer, A.; Beljonne, D.; Spano, F. C.; Cerullo, G.; Bardeen, C. J.; Schreiber, F. Robust singlet fission in pentacene thin films with tuned charge transfer interactions. *Nat. Commun.* **2018**, *9* (1), 954.
- (60) Eaton, S. W.; Shoer, L. E.; Karlen, S. D.; Dyar, S. M.; Margulies, E. A.; Veldkamp, B. S.; Ramanan, C.; Hartzler, D. A.; Savikhin, S.; Marks, T. J.; Wasielewski, M. R. Singlet exciton fission in polycrystalline thin films of a slip-stacked perylenediimide. *J. Am. Chem. Soc.* **2013**, *135* (39), 14701–14712.
- (61) Ramanan, C.; Smeigh, A. L.; Anthony, J. E.; Marks, T. J.; Wasielewski, M. R. Competition between singlet fission and charge separation in solution-processed blend films of 6,13-bis-(triisopropylsilylethynyl)pentacene with sterically-encumbered perylene-3,4:9,10-bis(dicarboximide)s. J. Am. Chem. Soc. 2012, 134 (1), 386–97.
- (62) Walker, B. J.; Musser, A. J.; Beljonne, D.; Friend, R. H. Singlet exciton fission in solution. *Nat. Chem.* **2013**, 5 (12), 1019–24.
- (63) Congreve, D. N.; Lee, J.; Thompson, N. J.; Hontz, E.; Yost, S. R.; Reusswig, P. D.; Bahlke, M. E.; Reineke, S.; Van Voorhis, T.; Baldo, M. A. External quantum efficiency above 100% in a singlet-exciton-fission-based organic photovoltaic cell. *Science* **2013**, *340* (6130), 334–7.
- (64) Yang, L.; Tabachnyk, M.; Bayliss, S. L.; Bohm, M. L.; Broch, K.; Greenham, N. C.; Friend, R. H.; Ehrler, B. Solution-processable singlet fission photovoltaic devices. *Nano Lett.* **2015**, *15* (1), 354–8.
- (65) Pazos-Outon, L. M.; Lee, J. M.; Futscher, M. H.; Kirch, A.; Tabachnyk, M.; Friend, R. H.; Ehrler, B. A Silicon-Singlet Fission Tandem Solar Cell Exceeding 100% External Quantum Efficiency with High Spectral Stability. ACS Energy Lett. 2017, 2 (2), 476–480.
- (66) Giri, G.; Verploegen, E.; Mannsfeld, S. C.; Atahan-Evrenk, S.; Kim, D. H.; Lee, S. Y.; Becerril, H. A.; Aspuru-Guzik, A.; Toney, M. F.; Bao, Z. Tuning charge transport in solution-sheared organic semiconductors using lattice strain. *Nature* **2011**, *480* (7378), 504–8.
- (67) Wong, C. Y.; Folie, B. D.; Cotts, B. L.; Ginsberg, N. S. Discerning Variable Extents of Interdomain Orientational and Structural Heterogeneity in Solution-Cast Polycrystalline Organic Semiconducting Thin Films. J. Phys. Chem. Lett. 2015, 6 (16), 3155–3162.
- (68) McDonough, T. J.; Zhang, L.; Roy, S. S.; Kearns, N. M.; Arnold, M. S.; Zanni, M. T.; Andrew, T. L. Triplet exciton dissociation and electron extraction in graphene-templated pentacene observed with ultrafast spectroscopy. *Phys. Chem. Chem. Phys.* **2017**, 19 (6), 4809–4820.
- (69) Dazzi, A.; Prater, C. B. AFM-IR: Technology and applications in nanoscale infrared spectroscopy and chemical imaging. *Chem. Rev.* **2017**, *117* (7), 5146–5173.